Appl Magn Reson (2017) 48:1273–1300
DOI 10.1007/s00723-017-0956-z

Applied Magnetic Resonance

ORIGINAL PAPER

High-Bandwidth Q-Band EPR Resonators

Rene Tschaggelar[1] · Frauke D. Breitgoff[1] · Oliver Oberhänsli[1] · Mian Qi[2] · Adelheid Godt[2] · Gunnar Jeschke[1]

Received: 1 August 2017 / Revised: 15 September 2017 / Published online: 23 September 2017
© Springer-Verlag GmbH Austria 2017

Abstract The emerging technology of ultra-wide-band spectrometers in electron paramagnetic resonance—enabled by recent technological advances—provides the means for new experimental schemes, a broader range of samples, and huge gains in measurement time. Broadband detection does, however, require that the resonator provides sufficient bandwidth and, despite resonator compensation schemes, excitation bandwidth is ultimately limited by resonator bandwidth. Here, we present the design of three resonators for Q-band frequencies (33–36 GHz) with a larger bandwidth than what was reported so far. The new resonators are of a loop-gap type with 4–6 loops and were designed for 1.6 mm sample tubes to achieve higher field homogeneity than in existing resonators for 3 mm samples, a feature that is beneficial for precise spin control. The loop-gap design provides good separation of the B_1 and E field, enabling robust modes with powder samples as well as with frozen water samples as the resonant behavior is largely independent of the dielectric properties of the samples. Experiments confirm the trends in bandwidth and field strength and the increased B_1 field homogeneity predicted by the simulations. Variation of the position of the coupling rod allows the adjustment of the quality factor Q and thus the bandwidth over a broad range. The increased bandwidth of the loop-gap resonators was exploited in double electron–electron resonance measurements of a Cu(II)-PyMTA ruler to yield significantly higher modulation depth and thus higher sensitivity.

Electronic supplementary material The online version of this article (doi:10.1007/s00723-017-0956-z) contains supplementary material, which is available to authorized users.

✉ Gunnar Jeschke
gunnar.jeschke@phys.chem.ethz.ch

[1] Laboratory of Physical Chemistry, ETH Zurich, Vladimir-Prelog-Weg 2, 8093 Zurich, Switzerland

[2] Faculty of Chemistry and Center for Molecular Materials (CM2), Bielefeld University, Universitätsstraße 25, 33615 Bielefeld, Germany

1 Introduction

The magnetic coupling of electron spins to the microwave field in electron paramagnetic resonance (EPR) spectroscopy is much weaker than the electric coupling on which optical spectroscopy relies. For that reason, resonators are used almost invariably in EPR spectroscopy to obtain a larger excitation magnetic field amplitude B_1 at given power as well as a larger signal amplitude at given transverse spin magnetization. The requirements on the resonator depend on the bandwidth of spin excitation and detection. The lower the required bandwidth is, the higher is the amplification of the microwave field B_1 that can be achieved. While the bandwidth in continuous-wave EPR can be reduced as far as the type of resonator, materials, and precision of machining allow, this does not apply to pulsed EPR experiments. For decades, pulsed EPR relied on excitation with monochromatic rectangular pulses. For such experiments, excitation bandwidth increases linearly with B_1 provided it is not limited by resonator bandwidth. However, at given microwave power incident on the resonator, a linear increase of B_1 can be achieved only at the expense of a square-root decrease of resonator bandwidth [1]. These two dependencies result in an optimal resonator bandwidth. The loss in sensitivity and in efficiency of converting microwave power to B_1 field amplitude that arises from larger required bandwidth can partially be compensated by concentrating the B_1 field in a smaller volume than is possible for the cavity resonators used in continuous-wave EPR. One of the most popular resonator designs for this purpose is the loop-gap resonator that was introduced for EPR spectroscopy at microwave frequencies by Froncisz and Hyde [2]. Dielectric resonators introduced by Walsh and Rupp [3, 4] are another popular choice. At Q-band (33–36 GHz) or higher frequencies, where wavelength limits the dimension of low-loss resonators, it can be advantageous to use oversized samples in cavity resonators [5–7]. In this case, part of the bandwidth increase results from microwave losses due to penetration of the electric field E into the sample. Although this is disadvantageous, the concomitant increase in sample volume and thus number of spins at given concentration can still lead to an increase in sensitivity.

During the past few years, the bandwidth limit of monochromatic rectangular pulses has been overcome by the advent of sufficiently fast electronics for generating frequency-swept and other shaped microwave pulses [8, 9]. This development changes the requirements on resonators. First, as the excitation bandwidth can be increased at given B_1 field amplitude by pulse shaping, optimal resonator bandwidth increases. The bandwidth limitation posed by the resonator on excitation can be partially relieved by the principle of offset-independent adiabaticity [10, 11], but resonator bandwidth needs to be adjusted to the required detection bandwidth. In Fourier transform EPR, experiments at X-band frequency signals could be detected over a band of 800 MHz, but were attenuated by the resonator at the band edges [12]. At Q-band frequencies, excitation could be achieved over a 2.5-GHz-wide band, but only at the expense of relatively slow sweeps at high microwave power at frequencies outside the nominal resonator bandwidth [13]. This strategy resulted in perceptible sample heating, which may

have been aggravated with the use of an oversized sample resonator with some penetration of the E field into the sample. Furthermore, it is expected and has been demonstrated that B_1 field inhomogeneity in the resonator compromises the precision of spin control by frequency-swept and other shaped pulses [14]. Clearly, the new technologies that have recently become available in pulsed EPR spectroscopy require the development of adapted microwave resonators. In this work, we demonstrate that the resonator design with multiple loops and gaps pioneered by Hyde's group [15] is suitable for such adaptation. We focus on Q-band (33–36 GHz) where sensitivity for many pulsed EPR experiments is better than in X-band.

This paper is structured as follows. We first discuss the basic theory that governs the relation between resonator bandwidth, power conversion, and resonator response in time domain. For reference to our previous Q-band resonator concept [5–7], we then show simulations of a TE_{102} box resonator for oversized samples with a 3 mm sample and with a 1.6 mm sample tube placed inside a 3 mm tube. The concept for the loop-gap resonators is outlined in Sect. 4.3. Then, the design and field simulations for three loop-gap resonators with 4–6 loops and gaps are presented in Sects. 4.4–4.6. In Sects. 4.7–4.8, the resonators are compared in simulation and experiment. The paper concludes with an application example comparing DEER measurements of a biradical of the type Cu(II)-PyMTA–spacer–Cu(II)-PyMTA in the TE_{102} box resonator with the corresponding measurements in loop-gap resonators.

2 Theory

Resonators are used in EPR to enhance sensitivity by storing the incoming microwave, thereby enhancing its B_1 field. The quality factor Q of a resonator is proportional to the number of wave periods stored in the resonator and describes the power multiplication in the excitation path as well as the signal multiplication in the receiving path. Q is defined as [1]

$$Q = \frac{2\pi(\text{energy stored in the resonator})}{\text{loss per cycle}}.$$

The time dependence of the fields in a resonator in the absence of an exciting wave can be described by the homogeneous differential equation

$$\frac{\mathrm{d}^2}{\mathrm{d}t^2}U + A\frac{\mathrm{d}}{\mathrm{d}t}U + CU = 0, \tag{1}$$

where U is the amplitude, the A-term describes losses and C is the usual quadratic potential for a harmonic oscillator. Assuming no losses, i.e., $A = 0$, Eq. (1) is solved by the harmonic oscillator:

$U = \mathrm{e}^{-i\omega_0 t}$ simplifies to $\sin(\omega_0 t)$, with the frequency $\omega_0 = \sqrt{C}$ in radians.

In case of non-zero losses, we set a damping factor $d = \frac{A}{2\omega_0} \ll 1$ (Fig. 1) and Eq. (1) changes to

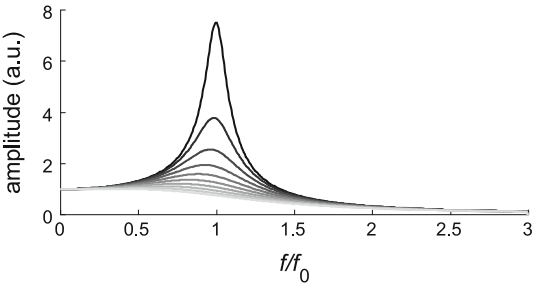

Fig. 1 Dampened resonance. Plotted here is $1/(\omega z)$ vs. the normalized frequency, with the damping d as parameter from 0.07 (black, largest amplitude) to 0.75 (gray, lowest amplitude). The smaller the loss, the higher the resulting amplitude, the taller the peak

$$\frac{\mathrm{d}^2}{\mathrm{d}t^2}U + 2d\omega_0\frac{\mathrm{d}}{\mathrm{d}t}U + \omega_0^2 U = 0. \tag{2}$$

A solution to Eq. (2) is

$$U(t) = U_0\,\mathrm{e}^{(-d\cdot\omega_0 t)}\ \sin\left(\sqrt{1-d^2}\omega_0 t + \varphi\right), \tag{3}$$

where φ is an arbitrary phase and U_0 is a constant. The resonance frequency is slightly decreased by the damping, according to

$$\omega_1 = \omega_0\ \cdot\ \sqrt{1-d^2}. \tag{4}$$

The exponential decay time constant $T = \omega_0 d = \frac{A}{2}$. The resulting Q value is $Q = \frac{1}{2d} = \frac{\omega_0}{A}$.

The losses A are from both dissipation and coupling. The dissipative losses define the unloaded Q_U, while the loaded Q_L is the unloaded Q_U parallel to the Q_C due to losses through the coupling hole:

$$\frac{1}{Q_\mathrm{L}} = \frac{1}{Q_\mathrm{U}} + \frac{1}{Q_\mathrm{C}}.$$

Since $d = \frac{1}{2Q}$, coupling of the resonator to the transmission line shifts the resonance frequency to lower frequencies.

We now consider the excited, dampened oscillator to describe the resonator coupled to a waveguide. In this case, the differential equation becomes inhomogeneous

$$\frac{\mathrm{d}^2}{\mathrm{d}t^2}U + 2\,d\,\omega_0\frac{\mathrm{d}}{\mathrm{d}t}U + \omega_0^2\,U = F_0\sin(\omega t), \tag{5}$$

where ω is the exciting frequency and F_0 the amplitude of the exciting wave. The steady-state solution is

$$U(t) = F_0\frac{\sin(\omega t + \phi)}{Z\omega}, \tag{6}$$

with the response function Z

$$Z = \sqrt{(2\omega_0 d)^2 + \frac{(\omega_0^2 - \omega^2)^2}{\omega^2}}, \tag{7}$$

$$\phi = \tan^{-1}\left(\frac{2\omega\omega_0 d}{\omega^2 - \omega_0^2}\right) + n\pi, \tag{8}$$

where n is an integer number and ϕ an arbitrary phase. Excitation of the resonator through the waveguide, therefore, dampens the amplitude according to the coupling and shifts the resonance frequency towards lower values. We omitted the influence of the coupler and the iris in this simplified model, which may result in another shift [16].

The quality factor Q_L of the resonator coupled to the waveguide is connected to the bandwidth Δf by definition.

$$Q_L = \frac{f_0}{\Delta f}, \tag{9}$$

where f_0 is the center frequency of the resonator. A low Q_L value, therefore, corresponds to a large bandwidth.

Excitation of spins in a time which is short compared to spin–spin interaction requires a large magnetic component B_1 of the microwave field. If we can assume a homogeneous B_1 field over the resonator volume V_r, B_1 is proportional to

$$B_1 = \sqrt{\frac{\mu_0 P_0 Q_L}{\pi f_0 V_r}}, \tag{10}$$

with the incident microwave power P_0 and the vacuum permeability μ_0. From Eq. (10) it follows that at the same incident microwave power and same bandwidth (same Q_L), a larger B_1 field can be obtained for a smaller resonator volume V_r. More specifically, a higher ratio between sample volume V_s and V_r, called the filling factor η, is favorable [1]. Equation (10) also implies an inverse relation between B_1 and the square-root of bandwidth that we mentioned in the Introduction. We aim to have Q_L as high as the required bandwidth permits to achieve a high B_1 field. Larger sensitivity is achieved if Q_L is reduced by over-coupling instead of by intrinsic losses of the resonator [17]. Hence, the resonator should have low internal losses, a high unloaded Q_L, and Q_L should be reduced by over-coupling to the required value.

As mentioned in the introduction, loop-gap resonators concentrate the B_1 field in a smaller volume than other resonators and thereby achieve high B_1 fields for a given incident microwave power [2, 18–20]. Loop-gap resonators consist of a conducting loop neighboring a gap which on its other side intersects with a second (larger) loop. The second, larger, loop carries the return flux of the B_1 field and is coupled to the waveguide. In a lumped-circuit description, a loop corresponds to an inductor and a gap corresponds to a capacitor [20]. A lumped-circuit equivalent network of a loop-gap resonator is shown in Fig. 2a.

Loop-gap resonators with Q-band frequencies were first reported by the Hyde lab [18]. Designs with more than one loop have been introduced, for example three-hole-two-gap structures for a spatially well-confined magnetic field and wide-band tuning [15]. By identifying the conducting surfaces adjacent to the sample tube as inductivities (loops), as is common in electronics, we use the nomenclature where a 'three-hole-two-gap' structure corresponds to a 'dual loop-gap' structure. In

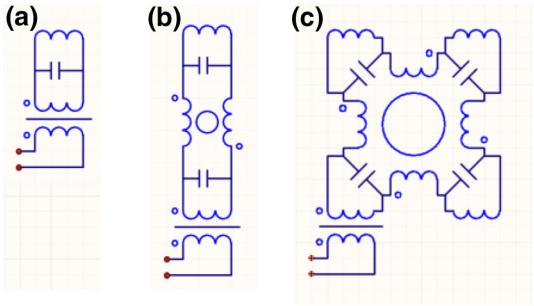

Fig. 2 Lumped circuit description for an **a** single, **b** dual and **c** quad loop-gap resonator coupled to a source

addition, commercial Bruker X-band split-ring resonators such as the MS3 resonator, which is popular for wide-band applications, are dual loop-gap resonators. Rectangular loop-gap resonators have been described as well. For example, the Hyde lab demonstrated rectangular X-band ENDOR resonators with 4, 6 and 8 gaps [21].

The previously existing loop-gap family of resonators [5] suffers from some drawbacks. First, the sample tube and the sample experience a significant electric field E. This leads to resonance frequency shifts depending on the amount, distribution and dielectric constant of the sample tube and sample in the immediate vicinity of the gap. Second, the frequency is highly dependent on the dimensions of the gap, rendering reproducible manufacturing challenging.

Oversized samples in cavity resonators, which have been introduced in the introduction, do not fulfil our quest for broadband resonators with high and homogeneous B_1 field either. Even though the larger sample volume was demonstrated to provide higher sensitivity in different applications for example for a 3 mm oversized sample box resonator [6, 7], the problem of E field experienced by the sample persists. Furthermore, the only moderate B_1 field homogeneity limits the precision of spin control and the larger sample volume reduces the B_1 at given incident microwave power compared to resonators for normal-sized samples which is detrimental for some types of experiments.

To overcome these limitations, we here introduce resonators with substantially larger bandwidth, higher B_1 field at given power and better homogeneity than the oversized sample box resonator. The improvement in homogeneity is expected to come at the cost of lower concentration sensitivity due to the smaller sample size. We test this proposition in the Application section. Since we aim for low E field in the sample volume, we do not expect large frequency shifts on introducing samples with different dielectric properties. Therefore, an ability to tune is not required. Other requirements to the resonator are ease of manufacturing with minimum mechanical parts as well as robustness. These resonators are tailored to wide-band pulsed EPR and thus over coupled by design.

3 Simulations and Experiments

The standard procedure for bandwidth characterization in electronics is to simulate the ratio S_{11} in amplitude and phase between the incoming and the outgoing wave. We found that optimizing the bandwidth experienced by an EPR sample in a resonator coupled to a waveguide based on S_{11} values is not feasible. The S_{11} value is dominated by the non-idealities of the coupler, its geometry and its reflections, whereas the actual field in the sample volume may or may not have a strong influence on this value. In our simulations, in many cases, S_{11} on-resonance was not even 3 dB lower than off-resonance. To overcome this problem, we characterized the B_1 field in the resonator in simulations with field probes after the identical calculations were performed for S_{11}. Note that these field probes are virtual (non-physical) and do not perturb the electromagnetic field distribution. We define a coordinate system where the *y*-axis is along the sample tube (center axis of the hole) and the *xz*-plane is the plane perpendicular to the *y*-axis at the center height of the structure. The *z*-axis is directed towards the gap. One field probe is placed in the origin of the coordinate system, i.e., in the center of the hole containing the sample tube. A second field probe is placed in the *xz*-plane at the inner surface ($x = 0.5$ mm) of the sample tube and a third probe on the *y*-axis at the upper end of the cylindrical hole containing the sample tube. Lacking physical point samples as well as means of precise positioning, we did not experimentally verify the simulated field at the individual point probes. Homogeneity of the B_1 field was assessed by exporting the complex B_1 vectors in an equidistant grid of 25 μm in the sample volume from simulations of the whole resonator with Microwave studio (see Sect. 6).

Experimentally, B_1 profiles were measured by nutation experiments [11]. The nutation frequency ν_1 is related to B_1 by $\nu_1 = \frac{g\mu_B B_1}{2\pi}$. The length of a pulse was incremented and inversion assessed by a subsequent Hahn echo sequence at the same frequency. This was repeated in steps of 20 MHz in a 1 GHz range around the expected center frequency f_0 of the resonator. At each step, the magnetic field was adjusted so that the resonance condition was maintained. This procedure provided the nutation frequency at each microwave frequency. Note that the total linearly polarized microwave field is described by $2B_1 \cos(\omega_{mw} t)$, since only one of the two circularly polarized components of the field drives transitions.

4 Results and Discussion

We simulated, built, and tested three loop-gap resonators with 4–6 loops and gaps (Table 1). They are referred to as quad loop-gap, pent loop-gap and hex loop-gap resonator. All three resonators are round cavities that enforce a low-loss TE mode. The B_1 field is focused to a central cylinder by a loop-gap structure. This confinement leads to a high filling factor. The active sample volume is limited by the height of the structure. The maximum B_1 field is expected to be inversely proportional to the structure height as the field is diluted to the volume of the sample

hole. The dominating single mode, which is also favored by the coupling rod, provides a strong and homogeneous B_1 field over a broad frequency range in all three loop-gap resonators.

4.1 TE_{102} Box Resonator for Oversized Samples

For comparison, we performed simulations for an oversized sample TE_{102} box resonator for 3 mm samples [6]. Simulations of the B_1 and E field are shown in Fig. 3a, b. The decrease in B_1 field towards the outer diameter of the sample is rather strong. The E field extends significantly inside the sample tube and inside the sample volume itself.

The B_1 field distribution over the sample volume is traced in Fig. 3c. B_1 includes a rather broad range of values at any horizontal slice through the resonator. The TE_{102} box resonator, therefore, shows rather low B_1 homogeneity over the sample volume. It has been shown that the volume parts with less B_1 field add to the echo nevertheless [6].

The frequency dependence of the B_1 field is shown in Fig. 3d for samples with varying dielectric constant ε. A strong shift in the center frequency f_0 with ε is apparent. f_0 shifts by approximately 580 MHz with a change in ε of 1. This reflects the presence of the E field inside the sample volume.

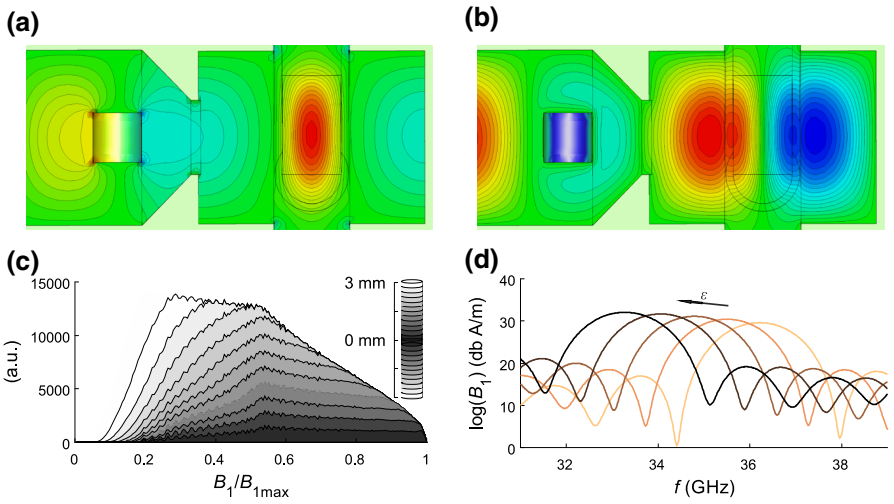

Fig. 3 Simulations for the oversized TE_{102} box resonator for a 3 mm sample with a dielectric constant of 5. The vertical position of the coupling rod is arbitrary and for reference only. **a** Projection of the B_1 field distribution/homogeneity on the center plane of the sample tube. The field is reduced to 10% at the inner surface of the sample tube. **b** Projection of the E-field on the center plane of the sample tube. The E-field enters the sample tube and, with increasing dielectric constant of the sample, also the sample volume. **c** B_1 field distribution/histogram stepped from the center plane upwards in 0.25 mm slices to 3 mm, shown cumulative. **d** B_1 field strength vs. frequency with the dielectric constant as parameter between 1 (light brown) and 5 (black). The frequency shifts strongly with the dielectric constant of the sample. Simulations predict a bandwidth of 1.6 GHz in the 33–36 GHz region, independent of the dielectric properties of the sample (color figure online)

In the simulations, the bandwidth of the mode around 33–36 GHz is 1.6 GHz for a sample with a dielectric constant ε of 5 in a 3 × 2.4 mm quartz tube. The B_1 field strength at the center frequency f_0 is 32 dB A/m with the current configuration at 1 W input. Experimentally, we measure a bandwidth of 150–350 MHz, depending on the coupler position, for a sample containing water/glycerol (See Fig S48 in the ESI). Overall, the bandwidth of the mode and its maximal B_1 are not strongly influenced by the coupler position. To summarize, the TE_{102} box resonator demonstrates rather strong B_1 inhomogeneity over the sample volume. The E field extends inside the sample volume, causing the center frequency f_0 of the mode to shift with the dielectric constant of the sample.

4.2 TE_{102} Box Resonator with 1.6 mm Sample

If the 3 × 2.4 mm quartz tube with the sample inside the TE_{102} box resonator is exchanged by a 1.6 × 1.1 mm quartz tube with sample, the E field penetrating the sample is strongly decreased. To counter the upward shift in frequency out of the range accessible with our spectrometer, we placed the 1.6 mm sample tube into a 3 mm tube. For the smaller sample, the B_1 inhomogeneity and the influence of the dielectric constant of the sample on the center frequency f_0 of the mode are largely reduced. Simulations of the B_1 and E field for a 1.6 mm sample within a 3 mm tube in the TE_{102} box resonator are shown in Fig. 4, together with illustrations of the B_1 field distribution over the sample volume and the frequency dependence of the B_1 field. All other geometric parameters for the simulations were the same as for the simulations in the previous section.

The outer sample tube still experiences considerable E field amplitude, yet the sample inside the smaller tube indeed experiences much lower E field amplitudes

Table 1 Resonator dimensions in mm

	TE_{102} box resonator	TE_{102} with 1.6 mm tube	Quad loop-gap	Pent loop-gap	Hex loop-gap
Resonator length × width	9.2 ×3.5	9.2 × 3.5			
Sample tube, quartz	3.0 × 2.4	1.6 × 1.1	1.6 × 1.1	1.6 × 1.1	1.6 × 1.1
Sample filling height h_S	Bottom + 4	Bottom + 4	6	6	6
Outer hole diameter			3.1	3	2.5
Gaps (length l_g × width w_g)			0.7 × 0.47	0.94 × 0.4	1.42 × 0.7
Resonator height h_R	7	7	9	8	8
Resonator diameter			9.3	11	12
Sample hole diameter			1.8	1.7	1.8
Iris (width × height)			0.9 × 7	1.2 × 6.2	1.3 × 6.5
Structure height			4	3.5	3.5

For all resonators, the coupling rod was a 2 × 2 brass tip on a movable 2 mm rexolite stick

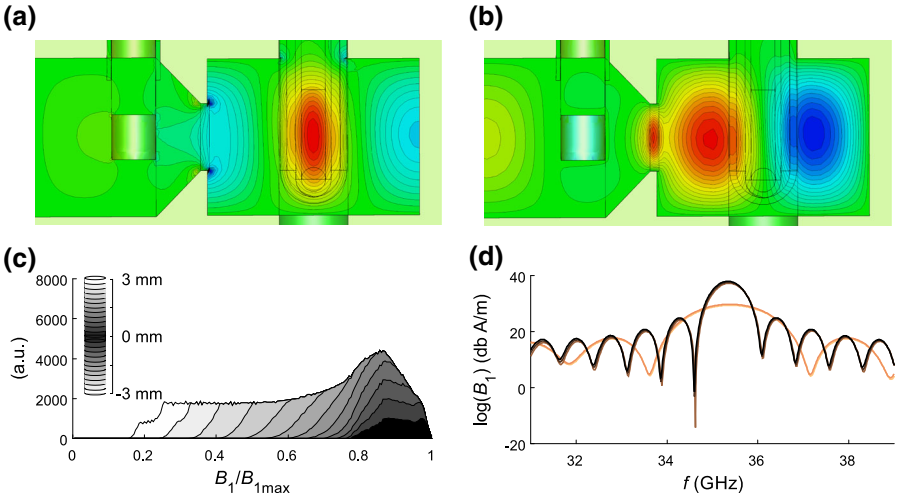

Fig. 4 Simulations for the oversized TE_{102} box resonator for a 1.6 mm sample with a dielectric constant of 5 in a 3 mm outer sample tube. The vertical position of the coupling rod is arbitrary and for reference only. **a** Projection of the B_1 field distribution/homogeneity on the center plane of the sample tube. **b** Projection of the *E*-field on the center plane of the sample tube. **c** B_1 field distribution/histogram stepped from the center plane upwards in 0.25 mm slices to 3 mm, shown cumulative. **d** B_1 field strength vs. frequency with the dielectric constant as parameter between 1 (light brown) and 5 (black). Due to the low filling factor and lower *E*-field penetration into the sample, the frequency shifts by only 30 MHz per unit step in the dielectric constant of the sample (color figure online)

(Fig. 4b). The B_1 field experienced by the sample inside the 1.6 mm tube is much more homogeneous (Fig. 4a, c). The simulation predicts a bandwidth of 1.59 GHz for $\varepsilon = 5$ and a B_1 field strength in the center with 30.7 dB A/m at 1 W input, as found for the 3 mm sample.

Comparison of the B_1 field distribution over the sample volume for the small sample (Fig. 4c) with the one for the 3 mm sample in the same resonator (Fig. 4c) shows that each of the horizontal slices parallel to the *xz*-center plane of the resonator experiences a much better defined B_1 field for the smaller sample. However, when considering all slices over the sample volume, the B_1 field is not very homogeneous (grayscale areas in Fig. 4c).

The center frequency f_0 for the maximal B_1 field remains roughly the same for any dielectric constant ε of the sample between 1 and 5 (Fig. 4d). Per unit change in ε in the simulations, f_0 only changes by approx. 30 MHz. This low shift partly reflects the lower *E* field experienced inside the sample volume and is partly due to the low filling factor.

For a 1.6 mm sample in the TE_{102} box resonator, the decrease in *E* field inside the sample volume dramatically improves the B_1 homogeneity and lessens the dependence of the center frequency f_0 of the mode on the dielectric properties of the sample. The smaller sample volume, however, leads to lower signal intensity, while the B_1 field is still significantly inhomogeneous and not as strong as it could be when focused to the sample volume. Therefore, we changed to the different resonator design outlined in the following.

4.3 Concept for Multi Loop-Gap Resonators

In a box resonator such as the oversized TE_{102} [6], the E field is strongly influenced by the sample tube with the sample and the B_1 field adapts. The B_1 field is rather inhomogeneous. A higher homogeneity than in the TE_{102} box resonator is achieved by spatially confining the fields by a conducting surface. Confining the B_1 field to a smaller volume also increases the power density and thus the maximum B_1 at given incident microwave power. At the same time, we have found in preliminary simulations a very confined E field leads to high Q_L values and accordingly a low bandwidth. Thus, the key is to confine the B_1 field and at the same time give the E field volume to expand.

A class of resonators with good spatial confinement of the B_1 field are loop-gap resonators [2]. However, our previously designed loop-gap resonators with one or two holes suffered from E-field at the sample tube and in the sample volume [5]. This led to strong resonance frequency shifts depending on the amount, distribution and dielectric constant of the sample tube and sample in the immediate vicinity of the gap. The frequency was highly sensitive to the dimensions of the gap, which made reproducible machining difficult. Lengthening or narrowing of the gap lowers f_0, as this corresponds to an increase of the capacitor. Thus, for a given frequency a shorter gap is narrower, and a longer gap is wider. The ratio between the diameter of the sample hole and the gap length l_g influences the homogeneity of the B_1 field. The useable trade-off range for these two connected parameters is limited, and for larger tube sizes the concept failed. For a single gap and a 1.6 mm sample hole, no combination of l_g and w_g can be found that provides sufficient homogeneity. Even with two gaps, only a poor homogeneity can be achieved. Basically, the capacitor cannot be made smaller without losing the metal that confines the E field. If the E field is not sufficiently confined, it enters the sample, if the B field is not sufficiently confined, the homogeneity is poor. Therefore, a new approach has been chosen to improve spatial separation of the E field and the sample. We reduced the capacitance, not by increasing the gap width or decreasing the gap length, but by placing multiple loops in series. Structures with 4–6 gaps were explored.

One aim was to design mechanically robust resonators that can be taken apart and cleaned easily. Another aim was reproducibility of the mechanical design. Therefore, we did set a lower limit for the gap width due to electro erosion of somewhat above 0.3 mm. We use wider gaps than in Refs. [22, 23] to achieve lower Q_L values. In preliminary simulations, narrower, shorter gaps provided less bandwidth and have thus not been considered.

The lumped-circuit description of loop-gap resonators with multiple gaps is shown exemplarily for the version with four gaps in Fig. 2c. Each gap is represented by a capacitor and each conducting segment confining the inner (sample) hole by an inductance. All inductances are coupled by the common magnetic field within the sample hole. The larger loops at the outer ends of the gaps (rims of the holes arranged around the central hole) are again represented by inductances. Coupling of the four outer loops to the neighboring outer loops has been omitted in the schematic. For the desired resonance, the four loops are acting synchronized. Modes

in which the outer loops resonate anti-phase to each other are by design well separated in frequency.

Since the resonators are designed for our dedicated wide-band pulse spectrometer and are not intended for continuous-wave EPR, they are over coupled by design.

Simulations, geometric dimensions and design for the three resonators are discussed individually in the Sects. 4.4–4.6.

4.4 Quad Loop-Gap

The design of the quad loop-gap resonator is shown in Fig. 5. This resonator consists of a cylindrical void space, where four holes and four gaps are arranged

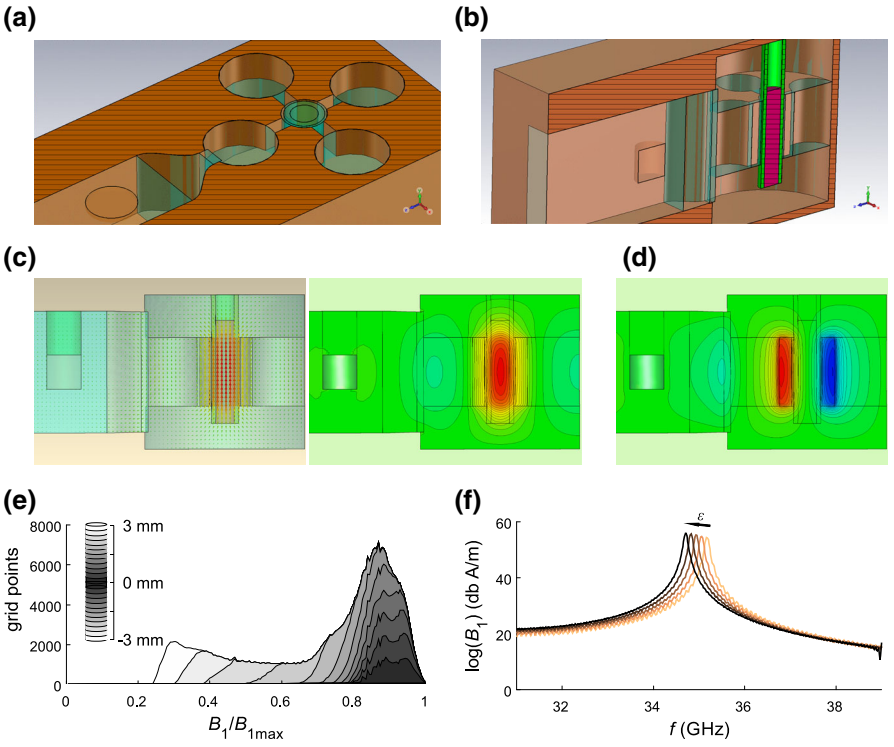

Fig. 5 Geometry and field simulations for the quad loop-gap resonator for a 1.6 mm sample with a dielectric constant of 5. **a** Top view. The cut plane is a fraction below the central plane to enable a 3D impression of the holes on the structure. In reality, the holes are higher than their diameter. **b** Cut through the center of the resonator. The vertical position of the coupling rod is arbitrary and for reference only. **c** Projection of the B_1 field distribution/homogeneity on the center plane of the sample tube as vectors and as intensity plot. **d** Projection of the *E*-field on the center plane of the sample tube. The *E* field penetrates into the sample tube, but very little into the sample itself. The maximum of the *E* field is concentrated towards the hole, away from the sample. The *E*-field vectors are perpendicular to this plane. **e** B_1 field distribution/histogram stepped from the center plane upwards in 0.25 mm slices to 3 mm, shown cumulative. **f** B_1 field strength vs. frequency with the dielectric constant as parameter between 1 (light brown) and 5 (black). The frequency shift is in the order of 120 MHz for a unit change in the dielectric constant of the sample (color figure online)

around the sample hole, thus creating four loop sections on the rim of the central hole. A loop gap resonator with four holes and four gaps has been designed by Sidabras and coworkers for W band [23]. The coupling of the resonator to the waveguide is magnetic, and is provided by an opening of one of the outer loops to the waveguide through an iris which is as high as the waveguide and 25% of the width of the waveguide. A coupler can be positioned at an adjustable height 2 mm in front of the end of the waveguide.

In Table 2, the response of the resonance frequency and bandwidth to changes in the geometric parameters are summarized for the three loop-gap resonators. The resonance frequency f_0 of the quad loop-gap resonator is influenced by the length l_g and the width w_g of the gaps, as well as the height of the cylindrical void space below and above the structure. In the immediate vicinity of the current configuration, the resonance frequency changes at a rate of 80 MHz/mm with the resonator height h_R. The quality factor Q_L and correspondingly the bandwidth are influenced by the width of the iris and the position of the coupler, yet not by the height of the resonator.

The B_1 field shown in Fig. 5c is much stronger than for the box resonator and homogeneous over the sample volume. This is also reflected in the histogram of the B_1 field distribution in Fig. 5e, where slices through the resonator in the xz-plane (center height) and 1.5 mm above and below exhibit a variation of $\pm$ 10% in the B_1 field (0.8–1 on a normalized scale).

Only for slices 1.75 mm or more above and below the xz-plane of the resonator, lower B_1 fields are experienced in the sample volume. Note, however, that these slices are at the limit or already outside of the structure height. Samples with a sample height of 3 mm ($\pm$ 1.5 mm on the y-coordinate), therefore, experience an extremely homogeneous and strong B_1 field, corresponding to the six darker gray shades in the B_1 field histogram. The B_1 field strength at f_0 at 1 W input ranges between 48 and 56 dB A/m, depending on the dielectric constant of the sample. This is about an order of magnitude higher than the maximal value for the TE_{102} resonator.

Extension of the E field into the sample volume (Fig. 5d) is rather low. Even though the E field penetrates into the quartz tube walls, the sample itself only experiences 20% of the maximal E field strength in the vicinity of the wall.

Table 2 Sensitivity of center frequency and quality factor Q_L on geometric parameters for the three loop-gap resonators

	Quad loop-gap	Pent loop-gap	Hex loop-gap
df_0/dl_g (MHz/μm)	7	5.4	6
df_0/dw_g (MHz/μm)	14	10.4	9.2
df_0/dh_R (MHz/mm)	80	140	40
dQ/dh_R for Q_{min}	0	0	0
$df_0/d\varepsilon$ (MHz)	120	85	60

Due to the small interaction of the E field with the sample volume, the resonance frequency of the resonator changes much less with the dielectric properties of the sample than was the case for the TE_{102} box resonator (compare Figs. 5f, 3d). While a unit change in the dielectric constant ε of the sample shifted the center frequency f_0 by 580 MHz in the TE_{102} resonator, in the quad loop-gap resonator this shift is merely 120 MHz. As was the case for the TE_{102} box resonator, the shape of the mode does not change with ε.

Simulations with $\varepsilon = 5$ predict a bandwidth between 90 and 560 MHz, depending on the coupler position. The simulations are compared to experimental results below.

4.5 Pent Loop-Gap

The geometry of the pent loop-gap resonator is shown in Fig. 6, together with simulations of the B_1 and E field. The central hole is surrounded symmetrically by five gaps connected to five outer holes. The coupling to the waveguide is magnetic as for the other resonators. In contrast to the quad loop-gap resonator, the width of the iris for the pent loop-gap resonator nearly corresponds to the width of the waveguide. The coupler position is 2 mm in front of the end of the waveguide as for the quad loop-gap resonator and can again be varied in the y-direction.

Changes in the length and width of the gaps induce a smaller change in the resonance frequency f_0 (Table 2) than in the case of the quad loop-gap resonator. In the immediate vicinity of the current configuration, the resonance frequency changes at a rate of 140 MHz/mm with the resonator height. Q_L is again influenced by the width of the iris and the position of the coupler and not significantly by the resonator height.

The B_1 field is relatively homogeneous over the sample volume (Fig. 6c) and the maximal value ranges between 43 and 47 dB A/m, depending on the dielectric constant of the sample. The relative change is similar to that in the quad loop-gap resonator. The field probe on the inner wall of the sample tube in the xz-plane measures a B_1 field 1.25 dB below the B_1 in the origin of the coordinate system (i.e., in the center of the resonator). Along the y-axis, the value at the upper boundary of the structure height is 2.5 dB lower than at the origin.

The distribution of B_1 field that the spins experience is slightly broader than for the quad loop-gap (Fig. 6e). As for the quad loop-gap resonator, sample areas above and below the 3.5 mm structure height experience significantly lower B_1 field amplitude than spins within the resonator.

Up to 20% of the maximal E field amplitude is experienced by the sample in the vicinity of the tube wall and E-field penetration into the sample volume is smaller than for the quad loop-gap resonator (Fig. 6d). This also reduces the shift of f_0 with the dielectric constant ε of the sample (Fig. 6f). With 85 MHz, the change in f_0 for a unit change in ε of one is only a third of the corresponding value for the quad loop-gap resonator.

Simulations with $\varepsilon = 5$ predict bandwidths between 890 and 1630 MHz, depending on the position of the coupler.

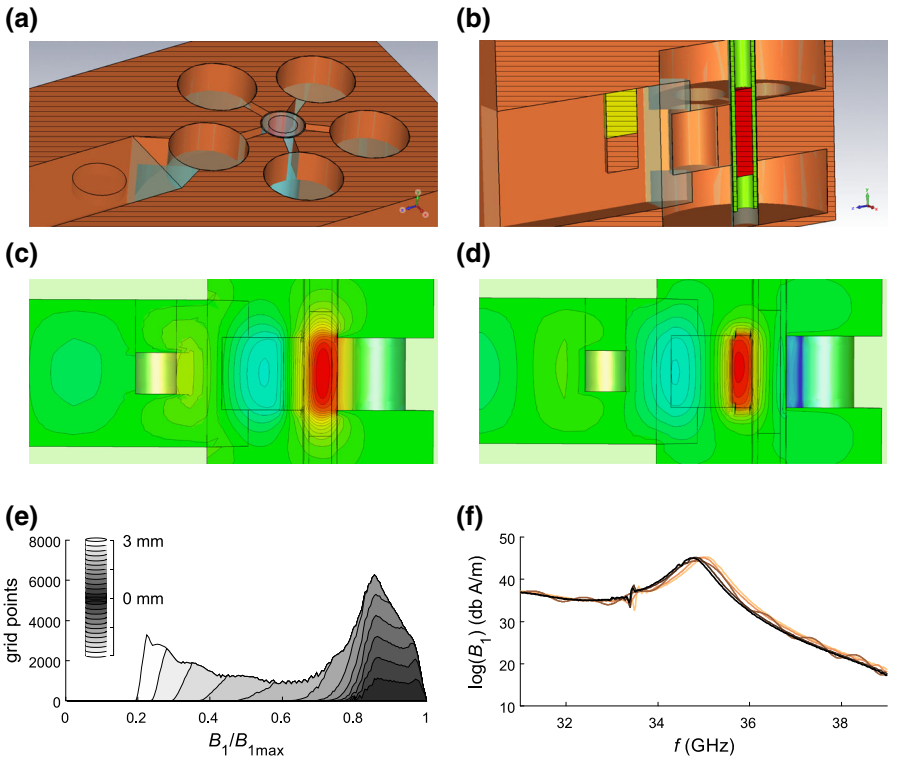

Fig. 6 Geometry and field simulations for the pent loop-gap resonator with a 1.6 mm sample with a dielectric constant of 5. **a** Top view. The cut plane is a fraction below the central plane to enable a 3D impression of the geometry. In reality, the holes are higher than their diameter. **b** Cut through the center of the resonator. The vertical position of the coupling rod is arbitrary and for reference only. **c** Projection of the B_1 field distribution/homogeneity on the center plane of the sample tube. The isolines are spaced at 6% of the maximum field, thus the homogeneity along the y-axis within the structure height is 65%. **d** Projection of the E field on the center plane of the sample tube. The E field penetrates into the sample tube and just very slightly into the sample itself. The maximum of the E field is concentrated towards the hole, away from the sample. **e** B_1 field distribution/histogram for horizontal slices through the resonator. Slices are from the center plane upwards in slices that get thicker by 0.25 mm. **f** B_1 field strength vs. frequency with the dielectric constant ε as parameter between 1 (light brown) and 5 (black) (color figure online)

4.6 Hex Loop-Gap

Design and field simulations for the hex loop-gap resonator are shown in Fig. 7. Analogously to the quad and pent loop-gap resonators, the outer holes and gaps are arranged symmetrically around the central sample hole. Again, the coupling to the waveguide is magnetic and the coupler is positioned at variable height 2 mm in front of the end of the waveguide. The iris is similar in width and height to the pent loop-gap design (Table 1) and, therefore, much larger than in the case of the quad loop-gap resonator.

In general, the same trends that were observed in the simulations for increasing the number of gaps n from 4 to 5 are followed when raising n further to 6.

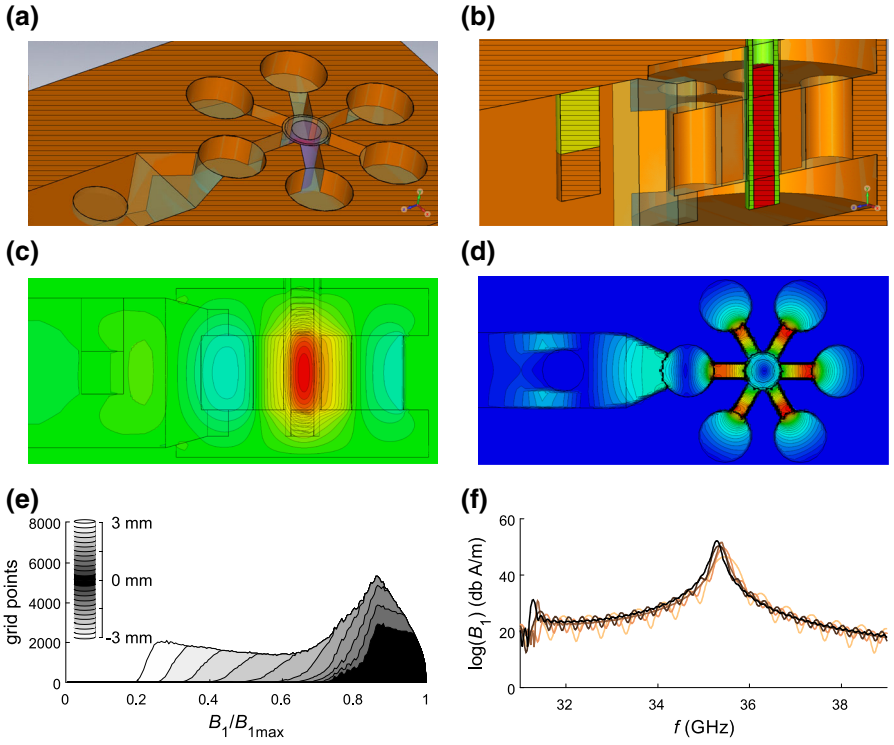

Fig. 7 Geometry and field simulations for the hex loop-gap resonator with a 1.6 mm sample with a dielectric constant of 5. **a** Top view. The cut plane is a fraction below the central plane to enable a 3D impression of the geometry. In reality, the holes are higher than their diameter. **b** Cut through the center of the resonator. The vertical position of the coupling rod is arbitrary and for reference only. **c** Projection of the B_1 field distribution/homogeneity on the center plane of the sample tube. The isolines are spaced by 6% of the maximum field, thus the homogeneity within the sample along the *y*-axis within the structure height is 70%. **d** Projection of the *E* field onto the horizontal center plane of the resonator. The *E* field is tangential within the center cut plane, in the structure, perpendicular to the sample tube. The *E* field is concentrated in the gaps, and the maximum is on the side of the outer holes, with a strong gradient towards the sample tube. The isolines are spaced by 6% of the maximum value. While the sample experiences fields of 20% of the maximum very close to the tube, within the quartz tube *E* fields up to 70% of the maximum are found. **e** B_1 field distribution/histogram for horizontal slices through the resonator. Slices start from the center plane ($y = 0$) and get thicker by 0.25 mm per gray shade. **f** B_1 field strength vs. frequency with the dielectric constant as parameter between 1 (light brown) and 5 (black) (color figure online)

The resonance frequency f_0 of the hex loop gap is the least sensitive against variations in the gap dimensions or resonator height of the three loop-gap resonators. The sensitivity to changes in the width of the iris and the position of the coupler on the quality factor Q_L remain the same.

The B_1 field (Fig. 7c) is slightly decreased in comparison to the quad and pent loop-gap resonators (39–52 dB A/m at 1 W input) and slightly less homogeneous (Fig. 7e), yet still much more homogeneous than in the TE_{102} box resonator. Field probes on the inner wall of the sample tube on the *xz*-plane and along the *y*-axis at the upper limit of the structure height measure B_1 attenuations of 1.25 and 2.5 dB,

respectively, compared to the resonator center. These ratios are the same as for the pent loop-gap resonator. As was the case for the resonators with lower number of loops, spins inside the 3.5 mm sample height experience a rather homogeneous B_1 field, while spins above and below the structure experience significantly lower and strongly varying B_1 fields.

The E field (Fig. 7d) is located in the gaps and concentrated at the outer gap ends. As the E field is distributed to more gaps, it extends less into the sample volume than in the quad and pent loop-gap resonators. This is also reflected in a smaller shift of f_0 with the dielectric constant ε of the sample of 60 MHz (Fig. 7f).

The simulations at $\varepsilon = 1$ and 5 predict bandwidths of 1.4 and 1.85 GHz, respectively, larger than for the quad and pent loop-gap resonators.

4.7 Comparison of Resonators by Simulations

To summarize, the following trends were observed in the simulations: (1) The distribution of the E field on more gaps reduces the E field amplitude penetrating into the sample volume. The sensitivity of the resonance frequency to the dielectric properties of the sample is thereby lowered. In comparison to the TE_{102} box resonator, the shift of the resonance frequency f_0 with the dielectric constant of the sample is much reduced in all three loop-gap resonators. (2) With distribution of the E field on an increasing number of gaps the bandwidth increases. (3) The increase in bandwidth Δf with the number n of gaps happens at the expense of a decreased B_1 field amplitude. This corresponds to expectations, as Q_L is inversely proportional to the bandwidth Δf and a variation in Q_L and B_1 are connected by Eq. (10). (4) B_1 field homogeneity decreases slightly with an increased number of gaps. Sample areas inside the 4 or 3.5 mm structure height experience a much more homogeneous B_1 field than the areas above and below.

4.8 Comparison of Resonators by Experiment

In Fig. 8, measurements of the resonator modes by nutation experiments are shown for the quad, pent and hex loop-gap resonator (from left to right). Experiments on coal at room temperature (Fig. 8a) are compared to measurements on a transmembrane peptide in a lipid bilayer in water/glycerol at 50 K (Fig. 8b). The position of the coupling rod was varied vertically between the upper end (blue) and the center height of the waveguide (red).

All three resonators show qualitatively the same resonator modes (bandwidth and ν_1) for both samples. The coupling rod allows the variation of the quality factor Q_L of the mode. At the highest coupler position, the lowest Q_L (highest bandwidth) is measured. Stepwise lowering of the coupling rod leads to an increase in Q_L until the maximal value is reached at a coupler height which corresponds to the middle of the coupler positioned at the center of the waveguide. If the coupler is lowered further, Q_L is slightly decreased again. The range of Q_L values obtained by fitting the experimental resonator profiles is summarized in Table 3 for all three resonators. The lower limit for Q_L decreases with increasing number n of gaps in the resonator. For the pent and hex loop gap resonators, we find Q_L values as low as 48,

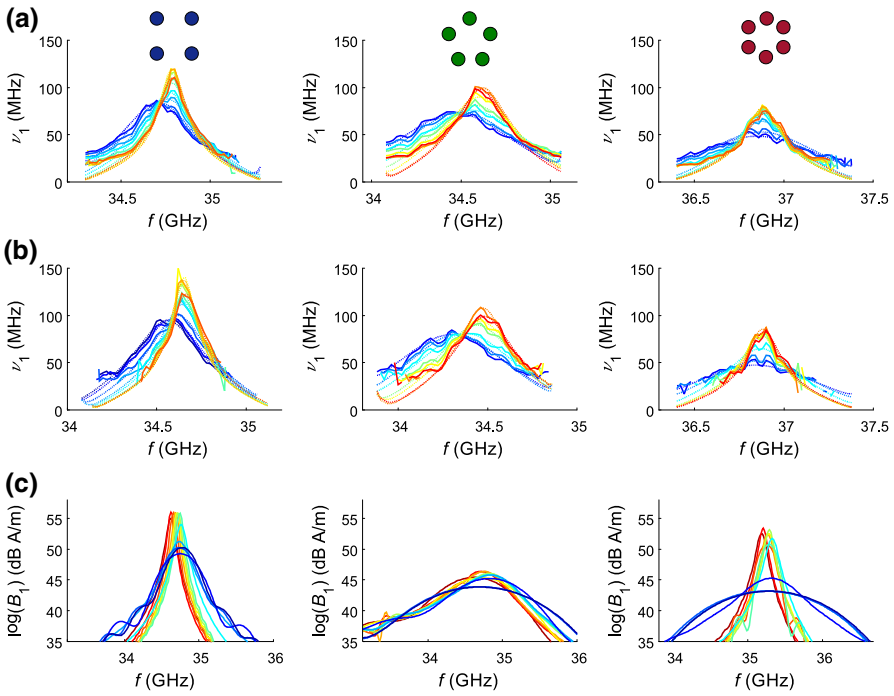

Fig. 8 Comparison of experimental and simulated resonator modes in the quad loop-gap (left), pent loop-gap (middle) and hex loop-gap resonator (right) at different positions of the coupling rod. Measurements of coal at room temperature (**a**), the transmembrane peptide WALP in water at 50 K (**b**) and simulations performed for a sample with a dielectric constant of 5 (**c**). The coupler position was changed from the upper end (blue) stepwise to the center height of the waveguide (red). Fits to the experimental profiles are overlaid as dashed lines (color figure online)

Table 3 Quality factors found in experiment and simulation

	Quad loop-gap	Pent loop-gap	Hex loop-gap
Exp. Q_L	95–260	50–130	48–210
Sim. Q_L	73–381	20–44	21–267

corresponding to bandwidths of about 700 MHz. In particular for the pent loop-gap, ν_1 exceeds 35 MHz over a range of about 1 GHz with a nominal 200 W output of the microwave amplifier. These Q_L values compare to a value of $\sim$ 180 previously reported for a dielectric Q-band resonator [4]. The upper limit for Q is 130 and 210 in the pent and hex loop-gap resonator, respectively, lower than in the quad loop-gap resonator. However, no monotonic trend is apparent, instead the modes observed in the hex loop-gap resonator resemble more closely the modes of the quad loop-gap resonator, albeit with a lower Q_L and B_1.

The trends in Q_L values found by fitting experimental results match simulations of B_1 at different frequencies f for $\varepsilon = 5$ and various coupler positions (Fig. 8c).

Even though the simulated value of B_1 cannot be directly compared to the experimentally measured values, since the latter depend on the actual microwave power incident at the resonator, similar tendencies are predicted: The broadest modes are found in the simulations for the coupler position at the upper end. The bandwidth increases dramatically from the quad to the pent loop-gap resonator and for the coupler positioned at the upper end the broad mode is replicated in the hex loop-gap resonator. For lower coupler positions, increasingly narrower modes are observed. However, for the pent loop-gap resonator no narrow-banded modes ($Q > 100$) are simulated, even though Q_L as high as 130 was found in experiments. Analogously to the experimental results, the maximum B_1 amplitude decreases with increasing number n of gaps in the resonator.

Due to the difference in the dielectric constant of coal and water/glycerol, the resonance frequency f_0 is slightly shifted between Fig. 8a, b. Note that, this frequency shift Δf_0 is partially due to the difference in temperature. To assess the frequency shift Δf_0 at the same temperature, the resonator frequency f_0 at 50 K for different samples was compared (data not shown). Δf_0 is with 320, 260 and 60 MHz in the quad, pent and hex loop-gap resonator, respectively, relatively small. The small Δf_0 in all three cases affirm that the influence of the E field in the sample volume is low. The decrease in Δf_0 for an increasing number n of gaps in the resonator confirm the simulations which predict a lower amount of E field penetrating the sample with increasing n.

The decreased influence of E field at the sample volume due to distribution on more gaps for the higher n resonators, therefore, correlates with increased bandwidth. In the ESI, the influence of the E field at various frequencies f is illustrated. More than half the bandwidth above and below f_0, the distribution of the E field on the n gaps becomes increasingly asymmetric. We tentatively assign the high bandwidth and correspondingly low Q_L values observed in the pent loop-gap resonator to the symmetric distribution of the E field over an outstandingly broad frequency range. In the experiment, the field distribution might not be quite as symmetric as in the simulations. This could explain the lower bandwidth and higher Q_L values observed experimentally than in the simulations.

The variation of B_1 with Q_L was explored for the different resonators. Based on the high homogeneity of the B_1 field in our simulations for the loop-gap resonators, we can assume a homogeneous B_1 field over the resonator volume. For this case, Eq. (10) is valid and rewriting it yields

$$\frac{B_1^2 f_0 V_r \pi}{\mu_0 P_0} = Q_L.$$

The left and right hand side of this equation are plotted against each other in Fig. 9. We thus expect a linear relation intersecting with the axes at the origin. Indeed, for each of the three loop-gap resonators the corresponding values observed for different coupler positions lie on a line. Light colors indicate values extracted from fits to measurements of coal, dark color fits to measurements of the transmembrane peptide. Deviations in B_1 between the coal and the transmembrane peptide sample might be due to different sample volumes. As the ensemble average

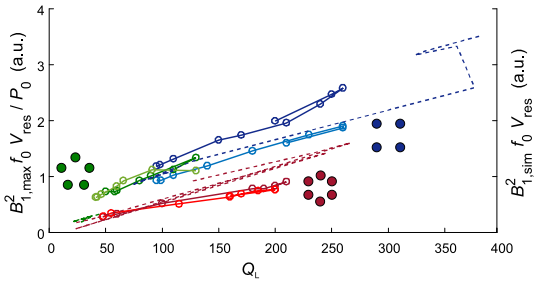

Fig. 9 Dependence of B_1 field amplitude on Q_L for the quad loop-gap (blue), the pent loop-gap (green) and the hex loop-gap resonator (red). Values from fits to measurements from coal at room temperature (light colors) and from a transmembrane peptide sample (dark colors) are shown. For comparison, values from simulations for an incident microwave power of 1 W are shown as dashed lines (color figure online)

is assessed by the experiments, the spins outside the resonator structure height lower the measured B_1 (compare Figs. 5e, 6e, 7e).

Between the three loop-gap resonators, the B_1 term can only be compared in a limited range due to the different range in Q_L values. Around $Q_L \approx 100$, a similar microwave field is achieved in the quad and in the pent loop-gap resonator, which is higher than in the hex loop-gap resonator. Therefore, a higher microwave field is available for a given incident microwave power P_0 at the same bandwidth in the quad and pent loop-gap resonators than in the hex loop-gap resonator. Note, that the B_1 field in the three loop-gap resonators does not show the same homogeneity. As this is assumed for Eq. (10), this limits quantitative comparison between the resonators.

Compared to the degree of agreement between experiment and simulation for the TE_{102} box resonator, the resonator modes of the loop-gap resonators are predicted rather well. In the case of the TE_{102} box resonator, simulations show a bandwidth of 1.6 GHz, while experimentally 150–350 MHz are observed for a sample containing water/glycerol (data shown in ESI). $B_1^2 f_0 V_r \pi / \mu_0 P_0$ values from fits of experiments in the TE_{102} box resonator with different coupler positions are included in the ESI as well. For the TE_{102} box resonator, the B_1 term does not show the same linear dependence on Q_L.

A direct comparison of the homogeneity of the B_1 field in the loop-gap resonators with the homogeneity in the TE_{102} box resonator was performed by recording nutation traces (Fig. 10). The sample of γ-irradiated quartz glass displays a narrow spectrum; thus the oscillation is not dampened by destructive interference of contributions with different frequency and Fourier transformation of the oscillation is not broadened by off-resonance effects. In the loop-gap resonators, long lasting oscillations are observed. In contrast, the modulation in the TE_{102} box resonator is strongly dampened and already decayed after a few oscillations. The damping is caused by destructive interference of oscillations with different frequency due to the distribution in B_1. Correspondingly, Fourier transformation of the data recorded in the TE_{102} resonators yields a peak with a full width at half maximum (FWHM) which is twice as broad as the FWHM for the loop-gap resonators (data not shown). Thus, the increased homogeneity in the loop-gap resonators was observed directly in

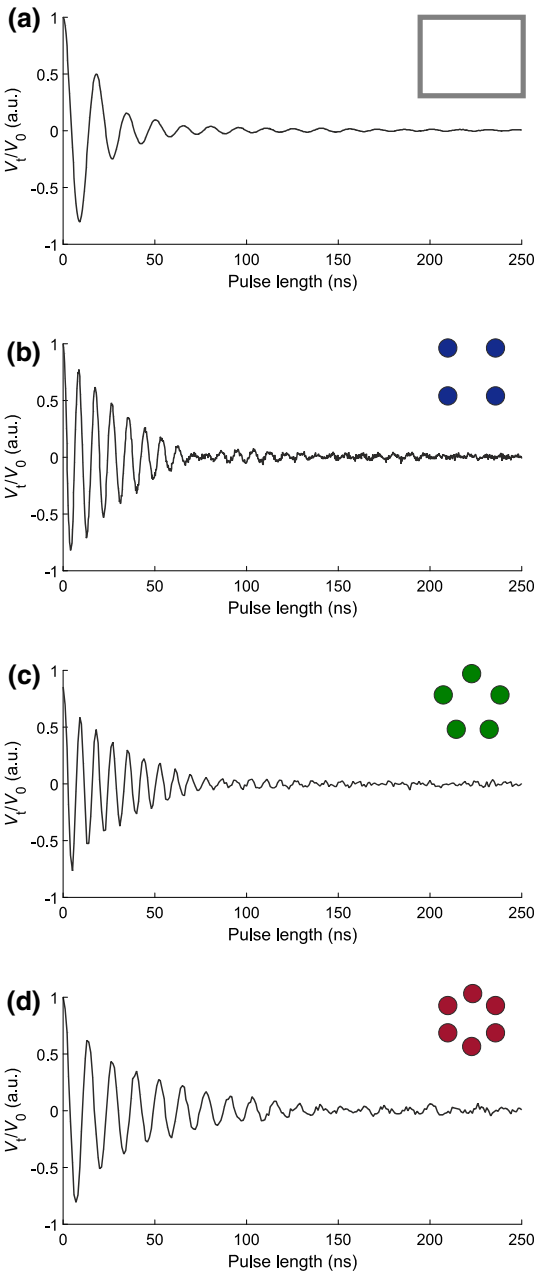

Fig. 10 Nutation traces measured from γ-irradiated quartz glass in the oversized TE_{102}, the quad-, pent- and hex loop-gap resonators. Due to the higher B_1 field homogeneity in the loop-gap resonators, the oscillation decays much slower than in the TE_{102} resonator

experiments. From simulations, the homogeneity was expected to be the highest in the quad loop-gap resonator. The nutation traces measured in the pent and hex loop-gap resonator appear to show even higher homogeneity, even though simulations suggested the opposite trend. The test sample used for the nutation experiments had

a height of only ∼ 1 mm, which might explain why the trend in homogeneity between the different loop-gap resonators expected from simulations was not observed.

4.9 Application

The increased bandwidth with high B_1 provided by the quad and pent loop-gap resonators was exploited in 4-pulse double electron–electron resonance (DEER) measurements of a Cu-PyMTA ruler (structure shown in Fig. 11), which consists of two Cu(II)–PyMTA complexes kept at a distance of ∼ 4.5 nm by a spacer of high stiffness [22, 24]. This complex corresponds to the Gd-PyMTA ruler $\mathbf{1}_5$ in [25]. DEER allows access to distance distributions in the nanometer range by time-dependent inversion at two different frequencies, conventionally called the observer and the pump frequency [26, 27]. Distance information is encoded in the modulation of the observed echo due to inversion of spins at the pump frequency. The sensitivity of the experiment thus depends on the amount of spins inverted by the pump pulse. The broad spectrum of copper(II) typically leads to very low modulation depth and thus low sensitivity when using conventional rectangular pump pulses because the excitation profile of such pulses is narrow with respect to the EPR spectrum [28]. Substituting rectangular pump pulses by shaped frequency-swept pulses allows access to inversion of more pumped spins and thus higher

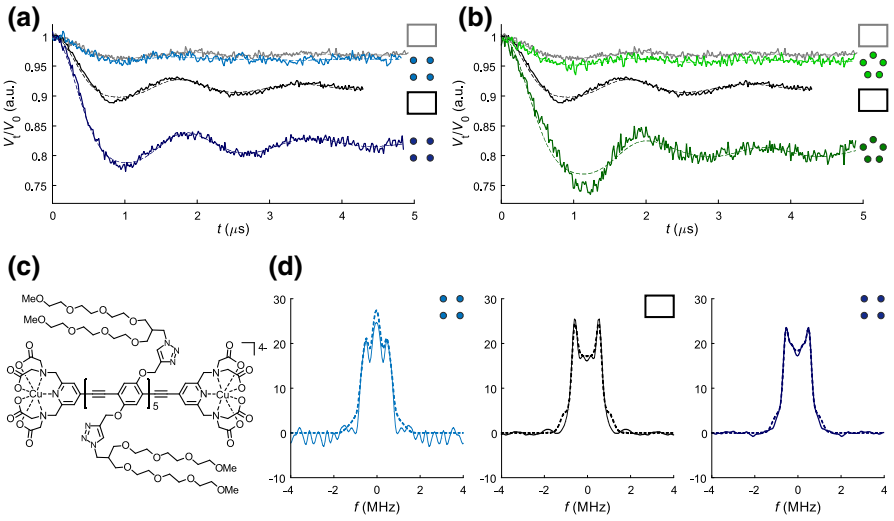

Fig. 11 Background-corrected 4-pulse DEER measurements with fits by DEER analysis (**a** and **b**) in the quad loop-gap resonator (light and dark blue), pent loop-gap resonator (light and dark green) and TE_{102} resonator (gray and black), structure of the Cu-PyMTA ruler (**c**) and the extracted dipolar frequencies for the quad loop-gap resonator compared to the TE_{102} resonator (**d**). Solid lines are experimental data, dashed lines fit by DeerAnalysis. Light colors: DEER measurements with rectangular pump pulses of 12 ns length; dark colors: measurements with frequency-swept HS{6,6} pump pulses with 100 ns length, 500 MHz bandwidth, 100 MHz offset from the observer frequency. The pump frequency and pump band, respectively, was above the observer frequency (color figure online)

sensitivity [11, 12]. The inversion efficiency of the pump pulse in turn depends on the bandwidth of the resonator.

In Fig. 11a, b, DEER measurements recorded from the Cu-PyMTA ruler in the quad loop-gap and the pent loop-gap resonators are compared to measurements in the TE_{102} box resonators with the same pulse settings. Pump pulses were either rectangular 12 ns pulses or shaped frequency-swept pump pulses, in particular sech/tanh (HS) pulses of order 6. HS pulses employ amplitude and frequency modulation by sech and tanh functions [9, 29]. HS pulses of higher order than 1 have been shown to achieve higher power efficiency than HS pulses of order 1 [10]. This proved useful to invert the maximal number of pumped spins in the case at hand, since the pulse duration of the pump pulse was limited to a fraction of the dipolar oscillation period [9] and a broad frequency band was desired. The observer frequency ν_{obs} was placed on the maximum of the copper(II) spectrum and the pump frequency (light colors) or pump band (dark colors) at higher frequency.

Modulation depth and sensitivity of all DEER traces are summarized in Table 4. Already with rectangular pump pulses but especially with the frequency-swept pump pulses, the modulation depth is considerably higher for measurements performed in the quad and pent loop-gap resonator than for measurements recorded with the same pulses in the TE_{102} resonator. For the HS pump pulses, the increase in modulation depth was—with the maximal power currently available from our 200 W traveling wave tube amplifier (TWT)—even on the order of 2. With the pent loop-gap resonator, an impressive modulation depth of 0.194 was achieved.

When rectangular pump pulses are used, similar sensitivities s were observed in the DEER measurements performed with the loop-gap resonators and with the TE_{102} resonator (Table 4). The sensitivity of DEER traces corresponds to the product of modulation depth and signal-to-noise ratio (S/N) as the useful signal is only the modulated part of the observed echo. The gain in modulation depth by utilizing the loop-gap resonators nearly compensated for the loss in signal intensity due to the smaller sample volume.

The sensitivity of the Cu(II)–Cu(II) DEER measurements with frequency-swept HS{6,6} pump pulses in the quad loop-gap resonator was significantly increased

Table 4 Modulation depth, noise and sensitivity estimate for Cu(II)-Cu(II) DEER measurements performed on the Cu-PyMTA ruler shown in Fig. 11 in the quad and pent loop-gap and the TE_{102} resonator, respectively

	Rectangular 12 ns			HS {6,6} above ν_{obs}		
	TE_{102}	Quad	Pent	TE_{102}	Quad	Pent
λ	0.031	0.037	0.040	0.088	0.190	0.194
Noise ($\times 10^3$)	3.4	4.7	5.0	3.8	5.2	8.0
$s = \lambda$/noise	9.1	7.8	8.0	23	36.7	24.3

Pump pulses are indicated. Sensitivity estimate was calculated as the modulation depth divided by the noise. The noise was approximated as the standard deviation of the difference between the background-corrected DEER trace and the fit by DeerAnalysis in the second half of the DEER trace

with respect to the measurements performed in the TE_{102} box resonator. Albeit measurements in the pent loop-gap resonator displayed an even higher modulation depth, the *S*/*N* was lower, causing a similar sensitivity with respect to the one of measurements in the TE_{102} box resonator. Note that, the strong frequency-swept pump pulses in the pent loop-gap resonator caused significant echo loss and a different pulse setup might be better for measurements in this resonator. As the hex loop-gap resonator provides access to a similar bandwidth as the quad loop-gap resonator, yet a lower B_1 field (Fig. 8), the sensitivity of Cu(II)–Cu(II) DEER measurements in the hex loop-gap resonator is expected to be lower than the sensitivity of the measurements in the quad and pent loop-gap resonators shown here.

An increase in modulation depth, as it was achieved with the quad and pent loop-gap resonators, is especially valuable for systems where measurement sensitivity is limited by constraints on the modulation depth. For example, biological systems where spin centers are introduced by ion exchange of naturally abundant metals can contain a large amount of unbound or unspecifically bound metal ions. An example is the substitution of magnesium by manganese in ATP:Mg^{2+}-fueled protein engines [30]. The high non-modulated part of the DEER trace in such a case strongly decreases the modulation depth whereas artifact intensities are maintained. For such systems, measurements in the loop-gap resonators presented here appear highly promising.

Furthermore, the increased number of pumped spins in the measurements performed in the quad loop-gap resonator decreases orientation selection. Orientation selection describes differences between the distribution of dipolar frequencies extracted from the experimental DEER trace to the one expected for an isotropic distribution of spin–spin vector orientations. The difference arises from excitation of only a subset of orientations of spin–spin vectors with respect to the external magnetic field [31]. The effect is observed by the deviation of the dipolar spectra (solid lines in Fig. 11d) from the fits by DeerAnalysis which assume an ideal powder-averaged Pake pattern that includes all possible orientations (dashed lines Fig. 11d). In particular, a missing outer shoulder in the Pake pattern is a good indicator for orientation selection. Orientation selection is generally expected in Cu(II)–Cu(II) DEER measurements at Q-band frequencies that are recorded at a single magnetic field due to the broad spectrum with respect to the bandwidth of the pulses [32]. The effect is observed especially strong in the measurements with rectangular pump pulses due to their narrow excitation profile, shown as example for the quad loop-gap resonator (light blue in Fig. 11d). Application of frequency-swept HS{6,6} pump pulses includes more orientations of the spin–spin vector with respect to the external magnetic field, therefore, the shape of the dipolar spectrum changes. The dipolar spectrum of measurements in the TE_{102} resonator with these pump pulses (black) resembles the ideal powder-averaged Pake pattern more closely, except for the missing outer shoulders. The same pump pulses in the quad loop-gap resonator yet again change the dipolar spectrum (dark blue). The outer shoulders of the dipolar spectrum are partially recovered, indicating the further increased number of orientations included in the dipolar spectrum.

5 Conclusions

Loop-gap resonators with 4–6 loops around a central hole were designed and tested for their B_1 field homogeneity, E field penetration of the sample, and bandwidth. All resonators proved to be less sensitive to the dielectric properties of the sample than a previously reported TE_{102} box resonator for oversized samples. They feature significantly better B_1 field homogeneity and, as expected due to the higher concentration of the B_1 field, much larger maximum B_1 field amplitudes than the box resonator. These resonators are intended for wide-band pulsed EPR experiments, and therefore, intrinsically over coupled. For the resonator with 5 gaps, the bandwidth can be varied between 270 and 700 MHz by shifting the coupler position, somewhat narrower bandwidths and correspondingly higher B_1 fields are attained with 4 outer holes. The resonator with 6 gaps did not feature a further increase in bandwidth and exhibited a relative loss in maximum B_1 compared to expectations.

Both simulations and experiment demonstrate good spatial separation of the B_1 and E field in all three resonators. With increasing number n of gaps, the E field in the sample volume decreases and the dependence of resonator frequency f_0 on dielectric constant ε, therefore, also decreases.

Despite the lower number of spins at given concentration in the active volume of the loop-gap resonators compared with the box resonator, DEER measurements on a Cu-PyMTA ruler showed improved sensitivity and significantly improved modulation depth when high-order hyperbolic secant pulses were used for the pump pulses. The moderate sensitivity loss in echo observation is more than compensated by the increase in modulation depth that becomes possible due to the larger bandwidth and higher B_1 field. In addition, the larger excitation bandwidth possible with the loop-gap resonators led to a reduction in orientation selection. The performance of the new resonators, in particular of the quad and pent loop-gap is encouraging the development of new ultra-wide-band EPR experiments at Q-band frequencies.

In general, this study shows that rational design of resonators guided by electromagnetic field simulations can provide good design leads, but that detailed performance may still differ between experiment and simulation, suggesting that several design leads should be built and tested.

6 Materials and Methods

The microwave fields in the resonators were simulated with CST Microwave Studio Version 2016. The B_1 field homogeneity was calculated as histogram of discretized field data, which was exported as ASCII from Microwave studio. Homogeneity was calculated by integrating the field for slices perpendicular to the sample tube. The slice starting at the center height of the resonator ($y = 0$) includes the highest B_1 field. An ensemble of approximately 360,000 points was used in the case of the loop-gap resonators and approx. 1.1 million points in the case of the 3 mm tube

inside the TE_{102} box resonator. For histograms, for the mode at resonance, the absolute peak value of the oscillating B_1 field was extracted, under the assumption that the vectors are in phase within the sample volume. The abscissa is 200 bins from zero to the normalized central field, while the ordinate contains the number of points in the corresponding bin. The ordinate is arbitrarily normalized.

All resonators were machined from a block of solid copper, in which the central hole structure was wire eroded to obtain a smooth and precise surface. An upper and lower lid complete the confinement of the microwave mode and suppress unwanted modes.

Measurements were performed with our home-built spectrometer [11] operated at Q-band frequency and featuring a 200 W microwave amplifier at a temperature of 20 K (Cu samples), 50 K (nitroxide samples) and room temperature (Coal), unless otherwise specified. Data analysis was performed using Matlab (version 2016b, The MathWorks Inc., Natick, MA, USA).

In general, the filling height of the sample tubes is limited to the upper limit of the resonator because a sample with a high dielectric constant which extends above the upper end of the resonator acts like a waveguide, thereby reducing the microwave power inside the resonator.

Resonator profiles were recorded as frequency-stepped nutation experiments with the procedure described in [11]. An ideal resonator profile H_{id} was fitted by least-squares minimization for every coupler position as

$$H_{id} = \left| \nu_{1,\max} \left(1 + iQ_L \left(\frac{f}{f_0} - \frac{f_0}{f} \right) \right)^{-1} \right|,$$

where $\nu_{1,\max}$ is the maximal nutation frequency, Q_L is the loaded Q factor, f the frequency and f_0 the center frequency of the mode. For the plot of the B_1 term over Q_L in Fig. 9, the parameters B_1, f_0 and Q_L determined from the fits were used and the sample volume for each resonator was calculated from the dimensions in Table 1. The incident microwave power P_0 was found experimentally to deviate less than $\pm$ 5% over the frequency range of the f_0 values. P_0 was, therefore, set to 1 for the traces from experimental data. Because the exact incident microwave power of the experiments was not determined, the simulation results were arbitrarily scaled to fit the experimental results.

The Cu-PyMTA ruler used in this study was prepared starting from the corresponding ruler precursor PyMTA-spacer-PyMTA (for the structural formula see ESI). This ruler precursor was prepared as described (ruler precursor **28_5** in [23]). The building block iodo-PyMTA needed for the assembly of the ruler precursor was obtained as described [32]. The ruler precursor (3.156 mg, 0.523 µmol) was dissolved in D_2O (750 µL). To this yellow solution, a solution of $CuCl_2$ in D_2O (0.05 M, 20.4 µL, 1.02 µmol) was added and the color of the solution changed to yellow-green. A solution of NaOD in D_2O (0.1 M, 35 µL, 3.5 µmol) was added to raise the pD of the solution to $\sim$ 8.2. The color of the solution changed to green. The solution was diluted with D_2O (501 µL) to obtain a 400 µM solution of the Cu-PyMTA ruler in D_2O. MS (ESI, negative ions): the most abundant m/z calculated for $[M]^{4-}$ $C_{282}H_{438}Cu_2N_{36}O_{106}{}^{4-}$, 1538.7; found, 1538.8.

For DEER measurements, the sample was further diluted with the cryoprotectant glycerol-d_8 to a 100 μM concentration.

DEER measurements were performed with the pulse sequence $\pi/2_{obs} - \tau_1 - \pi_{obs} - (\tau_1 + t) - \pi_{pump} - (\tau_2 - t) - \pi_{obs} - \tau_2$ where τ_1 was 400 ns and τ_2 5000 ns. DEER data were analyzed with DeerAnalysis, version 2016 [31]. Modulation depths (Table 4) were reported after fitting the background dimensionality, and selecting the regularization parameter by the L-curve criterion. Exceptions are the DEER traces recorded with rectangular 12 ns pump pulses, for which the background dimensionality was set to 3 due to the low signal-to-noise ratio.

The sensitivity s of DEER measurements was calculated according to

$$s = \frac{\lambda \cdot I}{n},$$

where λ is the modulation depth, I the signal intensity (1 due to normalization) and n the noise level. The noise level n was approximated as the standard deviation of the difference between the background-corrected DEER trace and the fit by DeerAnalysis (as shown in Fig. 11) in the second half of the DEER trace.

Acknowledgements We thank Andrin Doll and Stephan Pribitzer for helpful discussions and resonator tests on other applications. We are grateful to an anonymous reviewer for providing a derivation of Eq. (10) and correcting an error in constants in the original form of this equation. Funding by the Swiss National Science Foundation (grant no. 200020–169057) and by the German Science Foundation (DFG; SPP1601, GO 555/6-2) supported this work.

References

1. C. Poole Jr., *Electron Spin Rresonance—A Comprehensive Treatise on Experimental Techniques* (Dover Publications Inc., Mineola, New York, 1983)
2. W. Froncisz, J.S. Hyde, J. Magn. Reson. **47**, 515–521 (1982)
3. W.M. Walsh, L.W. Rupp, Rev. Sci. Instrum. **57**, 2278–2279 (1986)
4. A. Raitsimring, A. Astashkin, J.H. Enemar, A. Blank, Y. Twig, Y. Song, T.J. Meade, Appl. Magn. Reson. **42**, 441–452 (2012)
5. J. Forrer, I. García-Rubio, R. Schuhmam, R. Tschaggelar, J. Harmer, J. Magn. Reson. **190**, 280–291 (2008)
6. R. Tschaggelar, B. Kasumaj, M.G. Santangelo, J. Forrer, P. Leger, H. Dube, F. Diederich, J. Harmer, R. Schuhmann, I. García-Rubio, G. Jeschke, J. Magn. Reson. **200**, 81–87 (2009)
7. Y. Polyhach, E. Bordignon, R. Tschaggelar, S. Gandra, A. Godt, G. Jeschke, Phys. Chem. Chem. Phys. **14**, 10762 (2012)
8. P.E. Spindler, P. Schöps, W. Kallies, S.J. Glaser, T.F. Prisner, J. Magn. Reson. **280**, 30–45 (2017)
9. A. Doll, G. Jeschke, J. Magn. Reson. **280**, 46–62 (2017)
10. A. Tannus, M. Garwood, J. Magn. Reson. A **120**, 133–137 (1996)
11. A. Doll, S. Pribitzer, R. Tschaggelar, G. Jeschke, J. Magn. Reson. **230**, 27–39 (2013)
12. A. Doll, G. Jeschke, J. Magn. Reson. **246**, 18–26 (2014)
13. A. Doll, M. Qi, S. Pribitzer, N. Wili, M. Yulikov, A. Godt, G. Jeschke, Phys. Chem. Chem. Phys. **17**, 7334–7344 (2015)
14. G. Jeschke, S. Pribitzer, A. Doll, J. Phys. Chem. B **119**, 13570–13582 (2015)
15. R.L. Wood, W. Froncisz, J.S. Hyde, J. Magn. Reson. **58**, 243–253 (1984)
16. R.R. Mett, J.W. Sidabras, J.S. Hyde, Appl. Magn. Reson. **35**, 285–318 (2008)
17. G.A. Rinard, R.W. Quine, S.S. Eaton, G.R. Eaton, W. Froncisz, J. Magn. Reson. **108**, 71–81 (1994)
18. W. Froncisz, T. Oles, J.S. Hyde, Rev. Sci. Instrum. **57**, 1095–1099 (1986)

19. B. Simovič, P. Studerus, S. Gustavsson, R. Leturcq, K. Ensslin, R. Schuhmann, J. Forrer, A. Schweiger, Rev. Sci. Instrum. **77**, 064702 (2006)
20. M. Mehdizadeh, T.K. Ishii, J.S. Hyde, W. Froncisz, IEEE Trans. Microw. Theory Tech. **31**, 1059–1064 (1983)
21. W. Piasecki, W. Froncisz, W.L. Hubbell, J. Magn. Reson. **134**, 36–43 (1998)
22. R.R. Mett, J.W. Sidabras, J.S. Hyde, Appl. Magn. Reson. **31**, 573–589 (2007)
23. J.W. Sidabras, R.R. Mett, W. Froncisz, T.G. Camenisch, J.R. Anderson, J.S. Hyde, Rev. Sci. Instrum. **78**, 034701 (2007)
24. M. Qi, M. Hülsmann, A. Godt, J. Org. Chem. **81**, 2549–2571 (2016)
25. A. Dalaloyan, M. Qi, S. Ruthstein, S. Vega, A. Godt, A. Feintuch, D. Goldfarb, Phys. Chem. Chem. Phys. **17**, 18464–18476 (2015)
26. G. Jeschke, Annu. Rev. Phys. Chem. **63**, 419–446 (2012)
27. M. Pannier, S. Veit, A. Godt, G. Jeschke, H.W. Spiess, J. Magn. Reson. **142**, 331–340 (2000)
28. M. Ji, S. Ruthstein, S. Saxena, Acc. Chem. Res. **47**, 688–695 (2014)
29. M. Garwood, L. DelaBarre, J. Magn. Reson. **153**, 155–177 (2001)
30. T. Wiegand, D. Lacabanne, K. Keller, R. Cadalbert, L. Lecoq, M. Yulikov, L. Terradot, G. Jeschke, B.H. Meier, A. Böckmann, Angew. Chem. Int. Ed. **56**, 3369–3373 (2017)
31. G. Jeschke, V. Chechik, P. Ionita, A. Godt, H. Zimmermann, J. Banham, C.R. Timmel, D. Hilger, H. Jung, Appl. Magn. Reson. **30**, 473–498 (2006)
32. A.M. Bowen, C.E. Tait, C.R. Timmel, J.R. Harmer, in *Structural Information from Spin-Llabels and Intrinsic Paramagnetic Centres in the Biosciences*, vol. 152, ed. by C.R. Timmel, J.R. Harmer (Springer, Berlin, Heidelberg, 2013), pp. 283–327